

Designing a Matching Layer for Acoustic Sensors for the COUPP Dark Matter Detector

Justin P. Skycak, Marian High School

Mentor: Dr. Ilan Levine, Indiana University South Bend

May 11, 2013

Abstract

Although the existence of dark matter is supported by a variety of strong observational evidence, very little is known about its nature. The COUPP (Chicagoland Observatory for Underground Particle Physics) experiment attempts to detect dark matter by analyzing bubbles caused by particle collisions in a superheated liquid. Lead Zirconate Titanate (PZT) piezoelectric acoustic transducers are used to record acoustic emissions from the bubbles, which are used to identify the particles involved in the collisions. However, radioactivity of the PZT in the sensors also contributes to background which becomes dominant as COUPP detectors become more sensitive. If the design of these sensors can be improved, the number of sensors and the PZT mass per sensor needed to discern collisions can be minimized. The purpose of this project was to improve the sensitivity of COUPP's acoustic transducers by creating a matching layer with acoustic impedance between that of the fused silica quartz jar containing the superheated fluid and the PZT of the acoustic transducers. Cylindrical samples were made from various proportions of tungsten carbide powder and epoxy, and the density and speed of sound were measured and used to calculate each sample's acoustic impedance. A layer was cut from the sample with the correct acoustic impedance and its effect on acoustic transducer sensitivity was tested. Although current test results show that the matching layer damped the signal rather than amplifying it, there are several possible explanations for this outcome, and further testing is required.

Introduction

This report details a project to improve acoustic sensors used in the COUPP (Chicagoland Observatory for Underground Particle Physics) dark matter detection experiment at Fermilab. First, I will provide some background information to explain the significance and key concepts of my project. I will include sections regarding evidence for the existence of dark matter, attempts to detect dark matter (with a specific focus on the COUPP experiment), sound waves, why the acoustic sensors used in the COUPP experiment need to be improved, and how this can be done with a matching layer. I will then provide a detailed account of the procedure and data taken throughout the project.

Evidence for the Existence of Dark Matter

Humans are extremely visually-oriented beings: for a great deal of us, seeing is believing. This may explain many astronomers' skepticism when Swiss astronomer Fritz Zwicky discovered dark matter within the Coma cluster in 1933 [1,2]. However, the vast majority of scientists have come to accept the existence of dark matter as more recent studies have backed it with a plethora of evidence. Observations involving mass discrepancies in galaxies and clusters, cosmic background radiation, the structure of the universe, and the impact of big bang nucleosynthesis on baryon density all support the existence of dark matter.

Galactic mass-to-light ratios can be calculated using the orbital velocity law ($M = \frac{rv^2}{G}$, where M is the mass an object is orbiting, r is the orbital radius of the orbiting object, v is the object's velocity, and G is the universal gravitational constant) and the luminosity-distance formula ($L = 4\pi r^2 b$,

where r is the distance of the galaxy and b is the apparent brightness of the galaxy) and have led to the conclusion that galactic matter is mostly dark and does not contribute luminosity.

To calculate a galaxy's luminosity, the galaxy's apparent brightness and distance from Earth are needed. A galaxy's apparent brightness is calculated by simply measuring how bright it appears in the sky, and its distance can be determined from its velocity using Hubble's law ($v = Hr$, where v is the galaxy's velocity, H is Hubble's constant, and r is the distance of the galaxy). The velocity can be calculated by analyzing the Doppler shifts of its light emissions: a redshifted spectrum indicates that the galaxy is moving away from us, a blueshifted spectrum indicates that the galaxy is moving toward us, and the magnitude of the spectral shift determines the magnitude of the galaxy's velocity [1].

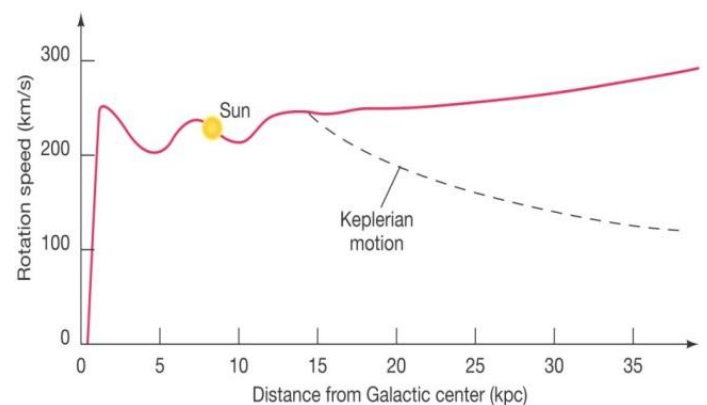


Figure 1: A rotation curve for the Milky Way galaxy. As the distance from the galactic center increases, the rotation speed slightly increases rather than decreases [3].

Because it gives the mass contained within an object's orbit, using the orbital velocity law to calculate the mass of a galaxy requires scientists to measure the velocity and orbital radius of the farthest objects orbiting the galaxy. The outskirts of spiral galaxies are comprised of hydrogen gas, and Doppler shifts in the spectra of hydrogen gas can be analyzed to determine the gas's velocity. Because the outskirts of spiral galaxies are very dark, the gas does not appear to orbit much more mass as its orbital radius increases. Therefore, its velocity should decrease as its orbital radius increases. However, this is not the case: even as the radius grows, the velocity of the gas remains roughly constant (see Figure 1). This indicates that even in the dark outskirts, farther objects orbit significantly greater the amounts of mass [1]. Galactic mass-to-light ratios as high as 50 solar masses per solar luminosity imply there is a greater amount of mass in galaxies than can be accounted for by luminous matter.

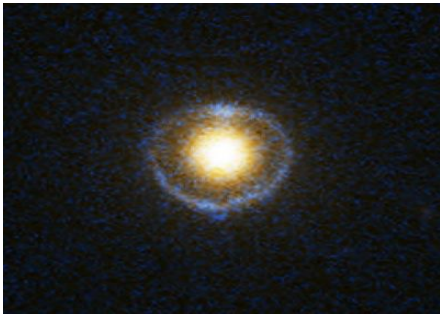


Figure 2: An Einstein Ring photographed by the Hubble space telescope [5].

Another method used to determine the mass of objects in space is gravitational lensing. Gravitational lensing occurs when gravity forces light to bend around a massive object, and the amount of light distortion can be used to calculate the light-bending angle. Since the light-bending angle depends on the strength of the gravitational force bending the light, and gravitational force depends on mass, the light-bending angle can be used to calculate the mass of the lensing object.

There are several types of gravitational lensing that can be used to for this purpose, such as strong lensing, weak lensing, and flexion. Strong lensing occurs when clusters and galaxies bend light to such an extent that it follows multiple paths around the lensing object. For example, an "Einstein Ring" forms when the background light comes from directly behind the gravitational lens (see Figure 2), and the radius of the ring is proportional to the square root of the mass of the lens. Even if the background light source is slightly off, the locations and distortions of the light can still be used to calculate the lensing object's mass. Weak lensing is caused by large-scale structures and although the light deflection is minimal, circular galaxies are often distorted enough that they appear as ellipses. The magnitude of distortion can be used to determine the total mass between the structure and the

observer (many different clouds of dark matter contribute to the weak lensing effect, not just a single lens). Flexion is caused by substructure and the outer areas of halos, and its amount of light distortion falls between that of strong and weak lensing. Although light is not deflected enough to make use of strong lensing mass calculation techniques and the observed area is on too small of a scale for weak lensing mass calculation techniques, there is a known relationship between mass and flexion distortion that can be used to mass the gravitational lens. Recent studies hold the mass-luminosity ratio calculations in accord with those derived from the orbital velocity law [1], providing more significant evidence for the existence of dark matter.

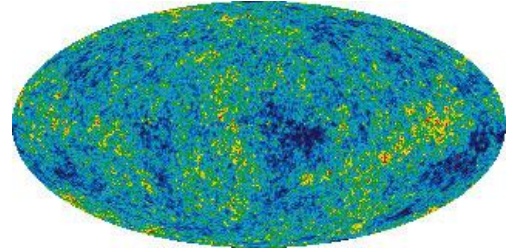


Figure 3: *Five Year Microwave Sky* by WMAP. The color differences represent temperature fluctuations in cosmic background radiation [6].

A careful analysis of local antimatter can provide evidence for the existence of dark matter as well, since many dark matter candidates are capable of pair-annihilating. The resulting radiation [7] can be detected by cosmic ray detectors such as the Pamela telescope, which observed more positrons than initially expected in cosmic radiation, and the Fermi Large Area Telescope, which discovered an even larger excess [8]. The Fermi Gamma Ray Space Telescope detected unique gamma ray emissions coming from our galactic center, and the Wilkinson Microwave Astronomy Probe (WMAP) discovered higher levels of microwave radiation near the center of Milky Way as well [9]. These discoveries of radiation may be attributed to pair-annihilation, which could point toward dark matter.

Additionally, WMAP discovered temperature fluctuations of 0.0002 Kelvin in cosmic background radiation [10] (see Figure 3), which indicates differences in temperatures [11] and densities [12] of clumps of matter in early universe. Using such fluctuations, scientists were able to conclude that the ratio of nonbaryonic matter to baryonic matter in the universe is approximately 6 to 1 [11].

Dark matter also plays an indispensable role in the structure of the universe. Although the universe is expanding, the space within galaxies tends to remain constant [1]. If baryonic matter had been the only type of matter, it would have been too hot to for these gravitationally bound systems to form in the time they did [13]. The gravity of dark matter would have been necessary to bring expanding matter together in this amount of time. It would have collected the first gas

clouds, which would have condensed to form stars within the dark matter halos, thereby explaining the constant velocities of objects orbiting increasingly farther from the center of galaxies and clusters. The process would have then repeated with galaxies to form clusters, and it is expected to repeat with clusters to form super-clusters. This matches what we see in the universe, and scientists have evidence that super-clusters are already beginning to form [1].

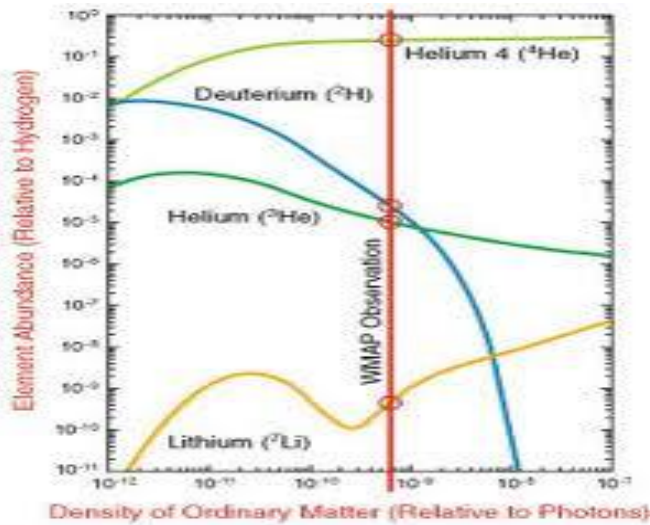


Figure 4: The abundance of elements created during the big bang is related to the density of ordinary matter in the universe [14].

Lastly, dark matter is supported by the well-tested and largely accepted theory of big bang nucleosynthesis. According to the theory, the big bang produced large amounts of helium-4 and smaller amounts of deuterium, helium-3, and lithium-7. Deuterium was not produced often after the big bang because it is weakly bonded and is easily blasted apart by gamma rays, so the current amount of deuterium must be the lower limit to the amount of deuterium produced by the big bang. Knowing the cosmic background radiation temperature and that deuterium production during the big bang depended on the total amount of baryonic matter [15] (see Figure 4), big bang nucleosynthesis predicts that baryonic matter accounts for 4% of the universe's critical density [16]. Since then, scientists have found that the total mass density of the universe is about 30% of the critical density [17]. This leaves a large amount of mass unaccounted for, which forms the basis of the Lambda-CDM model's assertion that dark matter constitutes about 25% of the universe's critical density [18].

Everywhere astronomers look, there is evidence for dark matter. Mass discrepancies in galaxies and clusters, cosmic background radiation, the structure of the universe, and big bang nucleosynthesis's impact on baryon density all reveal that although we can't directly see it, dark matter exists.

Detecting Dark Matter

Although the existence of dark matter is supported by a variety of strong observational evidence, very little is known about its nature. Several plausible dark matter candidates have been proposed, but their weak interactivity with normal matter makes them extremely difficult to detect. For this reason, the only known way to directly detect dark matter is to detect nuclei scattered by collisions and rule out all sources of nuclear recoils from known particles. Experiments such as XENON [19], CDMS [20], PICASSO [21], and COUPP [22] have attempted to detect and discriminate nuclear collisions using two-phase noble gas chambers, cryogenic detectors, liquid Freon droplet detectors, and bubble chambers.

The first step to identifying dark matter candidates was to determine whether the collisions are caused by baryonic matter or nonbaryonic dark matter. Baryonic matter, or "normal" matter, includes objects composed of quarks and leptons, the building blocks of atoms. The most likely baryonic candidates for dark matter, MACHOs (short for Massive Compact Halo Objects), can be faint red stars, brown dwarfs, or other Jupiter-size objects that don't emit large amounts of light [23]. They can be detected by gravitational microlensing, which occurs when a MACHO gravitational lens passes in front of a luminous object. The MACHO bends the background light, brightening distant stars for a short time [24]. Although MACHOs have been detected, there are not nearly enough to account for the mass of dark matter [23].

Unlike baryonic matter, nonbaryonic matter consists of particles we have yet to discover. In the past, the most considered nonbaryonic dark matter candidate was the neutrino. Neutrinos exhibit many of the characteristics displayed by dark matter—they are neutral and incapable of emitting electromagnetic radiation, and they only interact through the gravitational and weak forces [23]. However, being "hot," they move too quickly to clump into dark matter halos. This led to the proposal of WIMPs, or weakly interacting massive particles, which exhibit the aforementioned characteristics but are "cold" and move slowly enough to clump [23]. The most studied WIMP candidate is the neutralino, which is predicted by supersymmetry, a theoretical extension of the Standard Model that hypothesizes a heavier counterpart for every known particle. Neutralinos are plausible candidates for dark matter because they are heavy and neutral, emit no electromagnetic radiation, do not collide often, and are stable since they are the lightest supersymmetric particles [25].

Numerous dark matter searches attempt to directly detect WIMPs, and they all follow the same principle of creating a particle-scattering detection system and ruling out collisions due to known particles to discern dark matter. This is done by minimizing background radiation and utilizing a variety of methods to discriminate particle collisions. For example, cryogenic detectors use thermistors to measure

temperature changes which may be attributed to collisions between WIMPs and target nuclei, scintillation detectors analyze scintillation light which is emitted when electrons excited by collisions relax to lower energy states [26], ionization detectors detect charged ions formed by particle collisions, and bubble chamber detectors detect bubbles that form when a particle hits a nucleus of a superheated liquid and the recoiling nucleus loses kinetic energy as heat to the surrounding liquid [27]. Because so little is known about dark matter and the sensitivity required to detect it [28], it is essential that dark matter detectors are as sensitive as possible.

An excellent example of a dark matter search that pairs scintillation and ionization detecting techniques is XENON, which uses two chambers containing liquid xenon and gaseous xenon as a means to detect particle collisions. Such collisions can excite electrons in the xenon atoms, and the electrons emit scintillation light when they return to their original states [26]. Photomultipliers placed above the gas and below the liquid [30] then amplify the light to detectable levels [29]. Sometimes, if the collision is energetic enough, electrons are freed from their nuclear orbits. Although such an event does not emit light, an applied voltage moves the unbound electrons toward the xenon gas [29] where their charges can be detected. The charge-to-light ratio of an event is then used to determine whether it is an electronic recoil (from electrons or photons) or a nuclear recoil. To prevent radiation contamination, the xenon is continuously recirculated and purified [31]. Data from XENON100's 225 day collection has placed strict limits on dark matter characteristics [30], and the XENON collaboration plans to launch an improved detector, XENONIT, in 2015 [32].

In the Soudan Underground Laboratory in Minnesota [20], CDMS (the Cryogenic Dark Matter Search) attempts to detect WIMPs by detecting phonon and ionization signals within a detector crystal. When a particle collides with a nucleus in the detector, vibrations known as phonons propagate through the crystal and reach aluminum collector fins. The energy from the phonons is transferred to the aluminum electrons, which travel to and change the resistance of tungsten strips. This change in resistance can be amplified to make a detectable pulse. In addition to creating phonons, particle collisions in the detector can also result in ionization and free electrons. An applied voltage moves the electrons toward the crystal surface, where they are detected by a charge amplifier [33]. Cosmic radiation is suppressed by CDMS's underground location [20], and recoils are discriminated by the amount of ionization they produce and the shapes of the resulting phonon pulses [33]. CDMS has not been able to detect dark matter yet, but it has succeeded in setting more constraints on dark matter characteristics. Its most current experiment is SuperCDMS, which will eventually be moved 2 kilometers underground in SNOLAB to improve cosmic background suppression [20].

Launched in 2000 [25], PICASSO (Project in CAnada to Search for Supersymmetric Objects) searches for dark matter particles using millions of 50-100 micrometer liquid Freon droplets. These droplets are superheated so that the kinetic energy from particle collisions initiates bubble formation in the droplets. When the bubbles become large enough, they cause the droplets to pop. Although PICASSO's underground location and water cube barrier block much of the cosmic and neutron radiation, there is still some background that has to be accounted for. One method of discrimination involves analyzing the acoustic emissions when the droplets burst. Piezoelectric sensors are used to detect the emissions [28], and the type of particle involved in each collision can be determined from the amplitude of the resulting acoustic signal [34]. Another technique used to discriminate background radiation involves adjusting the temperature and pressure of the Freon droplets to adjust the bubble nucleation threshold, or the energy and length the energy needs to be released over to form a bubble [28]. Alpha particles are detectable above 15°C, neutralinos above 30°C, and gamma rays and other minimum ionizing particles above 50°C. To take advantage of this, the detector operates at different temperatures ranging from 20-47°C. Although PICASSO has not found evidence for any dark matter collisions, it has gathered enough information to help narrow down the characteristics of these mysterious dark matter particles [28].

Like PICASSO, the COUPP experiment (Chicago and Observatory for Underground Particle Physics) also employs explosive phase transition in superheated liquid. However, the COUPP experiment takes a slightly different approach. Rather than Freon droplets, COUPP uses superheated liquid CF_3I as a target for the collisions. The CF_3I is located in a fused silica bell jar in a pressure vessel surrounded by propylene glycol for pressure balancing. The kinetic energy transferred to C, F, or I nuclei in the collisions causes bubbles to form in the CF_3I [35].

The testing period begins with decompression for 5 seconds, which allows the CF_3I to superheat. Then, the pressure is stabilized for 30 seconds before the vessel enters a 500 second waiting period. If a bubble forms during this interval, the vessel is compressed for 30 seconds to keep it from expanding uncontrollably. If no bubbles are detected, compression occurs for 30 seconds at the end of the 500 second waiting period, and the cycle repeats [27].

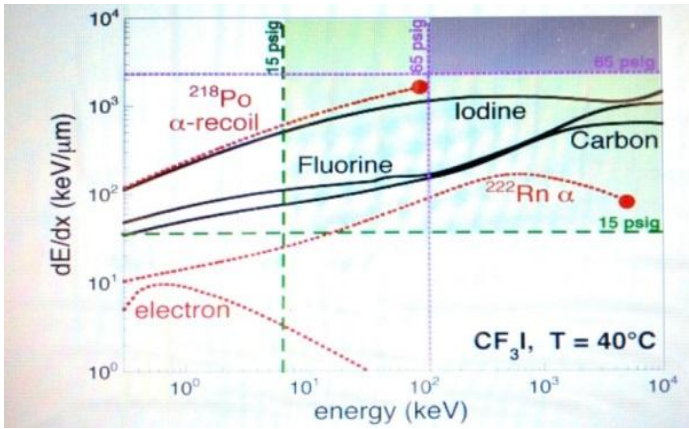


Figure 5: Dependence of bubble formation on total energy and stopping power [36].

In order to identify the bubbles caused by WIMP collisions, background has to be limited and recoils of known particles have to be identified. Background limitation is achieved by adjusting the temperature and pressure of the vessel [27] so only particles with large stopping power (energy deposition per unit length) (see Figure 5) are capable of fulfilling the bubble nucleation threshold and triggering bubbles [37]. COUPP's location 6800 feet underground (at SNOLAB near Sudbury, Ontario, Canada) provides a measurement area mostly free of cosmic ray background, but alpha emissions due to the radioactivity of some of the materials surrounding the CF_3I and in the rock walls still contribute to background radiation [27]. To discriminate the events, multiple characteristics of the bubbles are analyzed such as bubble location, the number of bubbles, and the acoustic emissions from the bubbles.

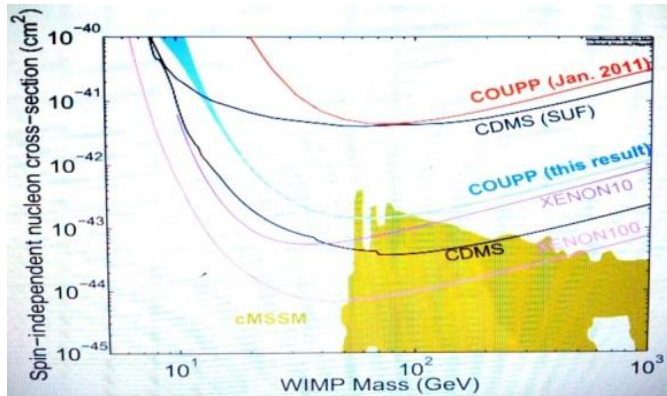


Figure 6: WIMP limits from recent dark matter searches [38].

Like XENON100, CDMS, and PICASSO, COUPP has not found evidence for dark matter collisions but has succeeded in setting new WIMP limits (see Figure 6) and plans to launch new and improved experiments [36].

Sound Waves

Waves are produced when elastic restoring forces and inertia cause vibrating atoms to oscillate, forming waves.

Because atoms can vibrate in a variety of different patterns, waves can take many forms.

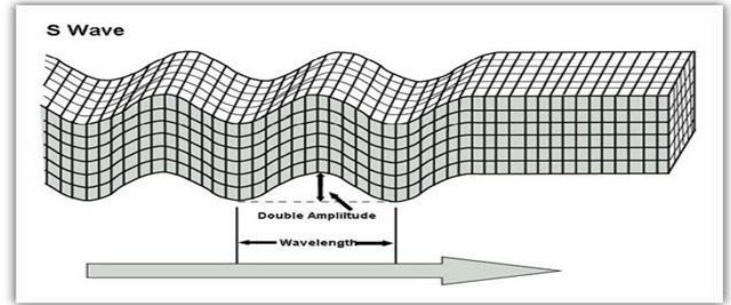
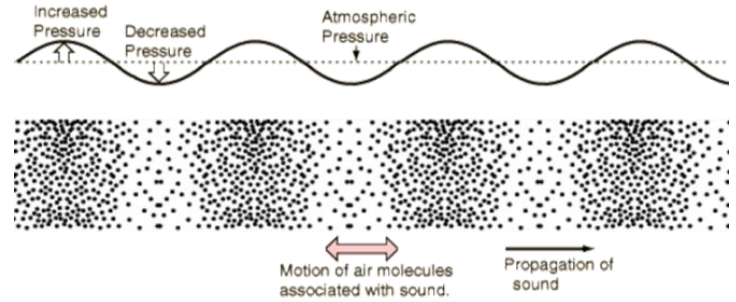


Figure 7 and Figure 8: The motion of longitudinal waves (top) [39] and shear waves (bottom) [40]

Longitudinal waves occur when the particles oscillate in the same direction as the wave, and they can propagate through both solids and liquids. Longitudinal waves (see Figure 7) are also known as “density waves” because they result in particle density fluctuations, or “compression waves” because they involve compression and rarefaction (expansion). In shear waves, the particles oscillate perpendicular to the direction of the wave (see Figure 8). These waves are weaker than longitudinal waves and can only propagate through solids.

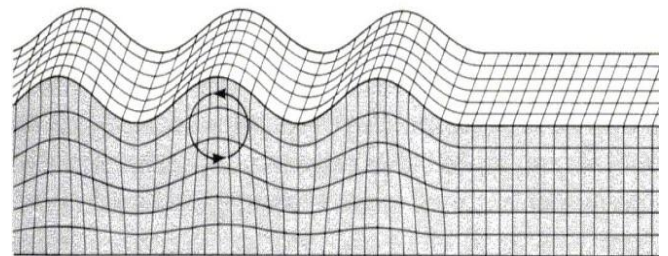


Figure 9: The motion of Rayleigh waves [41]

Surface waves, or Rayleigh waves, contain particles which move in symmetrical elliptical orbits (see Figure 9). They travel along the surfaces of solid materials, and the elliptical motions of the particles decrease with increasing depth. Lastly, plate waves travel parallel to the surfaces of materials only a few wavelengths thick. They propagate through the entire material and can be either symmetric or asymmetric (see Figure 10). Since wave oscillations can be described by Hooke's law, the speed of sound depends on the

medium of propagation, not the amplitude of the wave. Precisely, the square of the wave's velocity is equal to the elastic constant of the material divided by the density of the material [42].

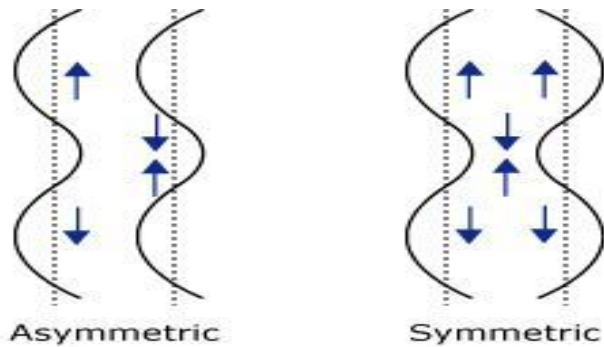


Figure 10: Asymmetric and symmetric waves [43].

There are many ways sound waves can interact with other objects and each other. Reflection, the cause of echoes [44], occurs when a sound wave passes from one medium to another and some of the sound reflects rather than passing through the boundary [42]. The amount of reflection depends on a medium's acoustic impedance, a measure of a material's resistance to sound propagation [44] which is equal to the product of the density of a material and the speed of sound through the material. Since the percent reflection (R) due to a change in medium is given by $R = \left(\frac{z_2 - z_1}{z_2 + z_1}\right)^2$ where z_1 and z_2 are the acoustic impedances of the two mediums, a greater acoustic impedance mismatch results in a larger amount of energy reflected [42]. Reflection also depends on the angle of incidence, or the angle between the wave and the perpendicular to the surface of the medium. Maximum reflection occurs at a 90° (normal) angle of incidence, and the percent reflection decreases as the angle of incidence becomes more oblique [44].

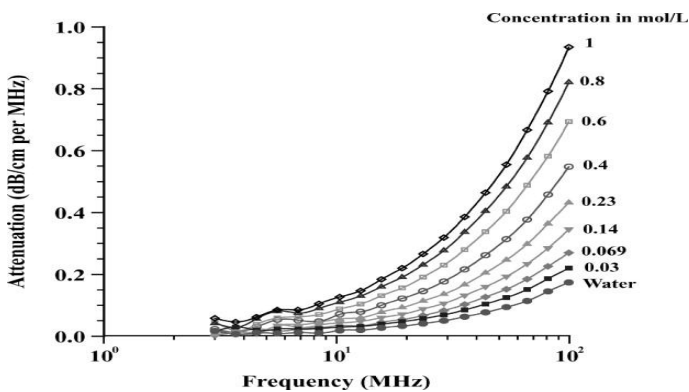


Figure 11: Frequency vs. attenuation in water with varying concentrations of CuSO_4 [45]. As frequency increases, attenuation increases. Increasing density causes increasing attenuation as well.

Attenuation occurs when a sound wave's intensity and amplitude decrease as it travels through a medium [44]. 20% of the lost energy is attributed to scattering, a reflection of sound in other directions [42] caused when a sound wave contacts a rough or irregular surface. Absorption, or the conversion of sound energy to other forms of energy (usually heat), accounts for the remaining 80% of the lost energy. Since a wave's frequency determines how fast its particles vibrate and particle vibrations release energy in the form of heat, attenuation increases as a wave's frequency increases (see Figure 11). This explains why low-frequency sounds (bass) travel more effectively than high-frequency sounds [44].

Unlike attenuation, focusing occurs when refraction, the bending of sound waves, redirects the waves in a way that increases their intensity and amplitude. Refraction happens at the boundary of two mediums when there is an oblique incident angle and different speed of sound in the two mediums. The oblique incident angle allows one part of the wave to enter the second medium before the rest of the wave, and the different speed of sound in the second medium either accelerates or slows down the wave. The combination of these two effects causes the wave to change direction [46].

Other effects of sound include diffraction and interference. Diffraction is the tendency of sound waves to bend around small objects and spread out beyond small openings. Interference occurs when waves traveling in the same medium line up. When waves are in phase, their amplitudes add, resulting in constructive interference. When waves are out of phase, their amplitudes subtract, resulting in destructive interference [46].



Figure 12: A sample Fourier analysis [47]. This sound wave has the most power at 332 Hz and 1258 Hz and has the least power at frequencies near 0 Hz.

Sounds can be measured and analyzed in a number of different ways. The intensity of a sound is its power per unit area [48], and it is determined by the sound's amplitude. Intensity is often measured in decibels (dB), with the difference in decibels equal to $10 \log \left(\frac{P_2}{P_1}\right)$ dB, where P_1 and

P_2 are the power measurements of two sounds and $P_1 < P_2$. In terms of volts, the difference in decibels is equal to $20 \log\left(\frac{V_2}{V_1}\right)$ dB, provided $V_1 < V_2$ [51]. Often, decibel measurements are taken relative to 1 Volt.

Using Fourier analysis, a sound can be analyzed by its frequency content. This is done by decomposing a sound waveform into sine and cosine waves with a Fast Fourier Transform and comparing the amplitudes of each harmonic [48] (see Figure 12).

Improving COUPP's Acoustic Transducers

A common tool used to detect sound is the acoustic transducer, which converts acoustic waves into electronic waves and vice versa. The most-used acoustic transducer is the piezoelectric type, which makes use of the piezoelectric effect to convert between electrical and mechanical energy [49], and the most common material used in these transducers is lead zirconate ceramics [42]. When pressure is applied to a piezoelectric material, the charges separate to form small dipoles and produce an electric field [49]. Alternatively, when an unstressed piezoelectric material is subjected to an electric field, dipoles form in the polarized material. This causes the unit cells to become slightly elliptical rather than spherical and results in deformation or “electrostriction” of the material [42].

The efficiency of a transducer is judged by the closeness of its input and output energies [50], and couplants and matching layers can be used to improve efficiency. Since air is a gas, its acoustic impedance drastically differs from those of solids and liquids, so a couplant is used to replace the air between two mediums. It minimizes the acoustic impedance mismatch, thereby reducing the amount of energy lost to reflection [42]. A matching layer has an acoustic impedance between those of the two mediums and a thickness of one-fourth the desired wavelength, and it is placed on the surface of the transducer to further minimize the acoustic impedance mismatch and reduce the amount of energy lost to reflection.

COUPP uses Lead Zirconate Titanate (PZT) piezoelectric acoustic transducers epoxied to the exterior of the quartz jar containing the CF_3I to record bubbles' acoustic emissions [27], and they have been shown to discriminate events induced by alpha decay from those caused by nuclear recoils to at least 99.3% purity. However, as COUPP detectors grow larger (COUPP aims to increase its sensitivity with a 500 kilogram detector [36]), the acoustic sensors themselves become potential sources of background radiation [38], so the number of acoustic sensors must be minimized. This can be done by improving the design of the transducers to minimize acoustic signal loss. Acoustic impedance mismatches between the fused silica quartz and the PZT manufactured by Virginia Tech cause much of the signal to be reflected rather than transmitted to the PZT transducers, and in order to maximize

the sensitivity of the acoustic transducers, an intermediate material with acoustic impedance between that of the quartz and the PZT can be placed between the quartz and transducer. This layer will ensure that that less reflection occurs and more of the signal is able to travel to the transducers.

Purpose

This leads to the purpose of my project: to create a matching layer which has an acoustic impedance between fused silica quartz and the PZT transducers made for COUPP by Virginia Tech. Samples with different acoustic impedances were made from varying amounts of MAS epoxy and tungsten carbide. The equation for acoustic impedance is $Z = \rho V$, and having more or less tungsten carbide in the sample changes both ρ and V . The density and speed of sound through each sample were measured, and these measurements were used to determine each sample's acoustic impedance. A thin wafer was cut from the sample with the correct acoustic impedance, and it was tested to see if it improved the acoustic transducer sensitivity.

Calculating the Goal Acoustic Impedance

The percent reflection from a medium of acoustic impedance Z_1 to a medium with acoustic impedance Z_2 is given by

$$R_{12} = \left(\frac{Z_2 - Z_1}{Z_2 + Z_1} \right)^2,$$

and the total percent reflection across both barriers is then given by

$$R_{\text{total}} = R_{13} + R_{32} - R_{13}R_{32}.$$

The total percent reflection is minimized when the acoustic impedance of the intermediate layer is equal to the geometric mean of the acoustic impedances of the surrounding media:

$$Z_3 = \sqrt{Z_1 Z_2},$$

where Z_1 and Z_2 are the acoustic impedances of the media surrounding the layer on each side. Since the acoustic impedance of the fused silica quartz used in the COUPP experiment is about 13 MRayl and the acoustic impedance of the PZT transducers made for COUPP by Virginia Tech is about 18 MRayl, the target acoustic impedance for a matching layer for the COUPP transducers was $\sqrt{13 * 18} = 15.2971 \approx 15$ MRayl. However, this was first simulated with transducers and glass on hand in the laboratory which had different impedances from those used in the COUPP detector.

Calculating the Densities of the Tungsten Carbide Powder and MAS Epoxy Mixture

The densities of the MAS epoxy and tungsten carbide powder were calculated to allow for conversions between volume and mass later in the experiment and to check whether a percent tungsten carbide by mass or a percent tungsten carbide by volume should be used, since air pockets in the powder may significantly contribute to its volume.

Calculating the Density of the Tungsten Carbide Powder

To calculate the density of the tungsten carbide powder, a graduated cylinder was filled with tungsten carbide powder, and the mass of the tungsten carbide powder was calculated by subtracting the mass of the empty graduated cylinder from that of the filled graduated cylinder. The mass of the tungsten carbide powder and the volume of the tungsten carbide powder were then used in the tungsten carbide powder density calculation, which yielded $10.4 \pm 0.1 \text{ g/cm}^3$ (see Tables 5 and 6).

Measured Quantity	Measurements	Average
Mass of empty graduated cylinder	41.19 g, 41.18 g, 41.18 g; all $\pm 0.01 \text{ g}$	41.18 $\pm 0.01 \text{ g}$
Volume of tungsten carbide powder	$10.0 \pm 0.1 \text{ cm}^3$	10.0 $\pm 0.1 \text{ cm}^3$
Mass of filled graduated cylinder	145.08 g, 145.09 g, 145.08 g; all $\pm 0.01 \text{ g}$	145.08 $\pm 0.01 \text{ g}$

Table 5: Volume of tungsten carbide powder and masses of filled and empty graduated cylinder.

Calculated Quantity	Expression	Result
Mass of tungsten carbide powder	$\frac{\text{mass of filled graduated cylinder}}{\text{mass of empty graduated cylinder}}$	103.90 $\pm 0.02 \text{ g}$
Density of tungsten carbide powder	$\frac{\text{mass of tungsten carbide powder}}{\text{volume of tungsten carbide powder}}$	$10.4 \pm 0.1 \text{ g/cm}^3$

Table 6: Mass and density calculations for tungsten carbide powder.

The density calculations of $10.4 \pm 0.1 \text{ g/cm}^3$, which fell below the accepted values of 11.25 g/cm^3 for tungsten carbide powder and 15.8 g/cm^3 for solid tungsten carbide (not powder). This means that air pockets occupied a significant amount of volume in the powder (the company made the powder settle more before they measured its volume). Because the air pockets contributed strongly to the volume of the powder but had a negligible mass contribution, the percent

tungsten carbide in the samples was first calculated as a percent by mass instead of a percent by volume.

Calculating the Density of the MAS Epoxy Mixture

The density of the MAS epoxy mixture (two parts resin, one part hardener) was calculated using two different methods to ensure accuracy. First, a pure MAS epoxy sample was massed with a scale and the volume of the sample was calculated by observing how much water it displaced in a graduated cylinder (see Figure 14 and 15 and Tables 7 and 8). The density of the MAS epoxy mixture was calculated by dividing the mass of a pure epoxy sample by its volume (see Table 9).

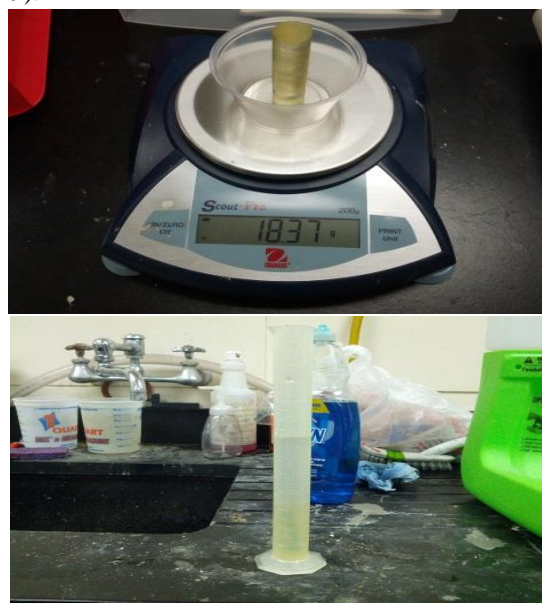


Figure 14 (left) and Figure 15 (right): Measuring the mass and volume of a pure epoxy sample.

Water Displacement Test	Initial Volume	Final Volume	Sample Volume final volume – initial volume
1	60.6 $\pm 0.1 \text{ cm}^3$	76.9 $\pm 0.1 \text{ cm}^3$	$16.3 \pm 0.2 \text{ cm}^3$
2	54.3 $\pm 0.1 \text{ cm}^3$	70.6 $\pm 0.1 \text{ cm}^3$	$16.3 \pm 0.2 \text{ cm}^3$
3	50.0 $\pm 0.1 \text{ cm}^3$	66.5 $\pm 0.1 \text{ cm}^3$	$16.5 \pm 0.2 \text{ cm}^3$

Table 7: Water displacement measurements for the pure epoxy sample.

<u>Measured Quantity</u>	<u>Measurements</u>	<u>Average</u>
Mass of pure epoxy sample	18.37 g, 18.37 g, 18.37 g; all ± 0.01 g	18.37 ± 0.01 g
Volume of pure epoxy sample	16.3 cm ³ , 16.3 cm ³ , 16.5 cm ³ ; all ± 0.2 cm ³	16.4 ± 0.2 cm ³

Table 8: Mass and volume measurements and averages for the pure epoxy sample.

<u>Calculated Quantity</u>	<u>Calculation</u>	<u>Result</u>
Density of pure epoxy sample	$\frac{\text{mass of pure epoxy sample}}{\text{volume of pure epoxy sample}}$	1.12 ± 0.01 g/cm ³

Table 9: Density calculation for the pure epoxy sample.

The second method used to calculate the density of the MAS epoxy mixture involved a calculation using the densities listed on the labels of the resin and hardener containers (see Tables 10 and 11).

<u>Substance</u>	<u>Density Found on Container</u>
MAS Epoxy Resin	9.2 lb/gal = 1.10 g/cm ³ (at 77 deg. F)
MAS Epoxy Hardener	1.08 g/cm ³ (at 77 deg. F)

Table 10: Densities listed on the resin and hardener containers.

<u>Calculated Quantity</u>	<u>Calculation</u>	<u>Result</u>
Density of pure epoxy sample	$\frac{2}{3}$ (density of resin) + $\frac{1}{3}$ (density of hardener)	1.1 g/cm ³

Table 11: Density calculation for the pure epoxy sample.

The calculations from the two different methods were extremely similar - equivalent, actually, when rounded to 2 significant figures. The result of 1.1 g/cm³ was used as the density for the pure epoxy mixture.

Making the Samples

First, molds were created for each sample. A plastic tube was cut to 12 cm, the ends were filed, and rubber stoppers were placed in each end (see Figure 16).



Figure 16: An empty sample mold

The required masses of MAS epoxy resin, MAS epoxy mold, and tungsten carbide powder were measured out in plastic cups using a scale that was zeroed to each cup (see Table. 12). The required masses were calculated in excess to ensure that there would be enough mixture to fill each sample mold.

<u>Mass of Epoxy Resin</u>	<u>Mass of Epoxy Hardener</u>	<u>Mass of Tungsten Carbide</u>	<u>Percent Tungsten Carbide by Mass</u>
36 \pm 1 g	18 \pm 1 g	0 g	0%
20 \pm 1 g	10 \pm 1 g	45 \pm 1 g	60 \pm 4%
20 \pm 1 g	10 \pm 1 g	70 \pm 1 g	70 \pm 3%
20 \pm 1 g	10 \pm 1 g	120 \pm 1 g	80.0 \pm 2.3%
20 \pm 1 g	10 \pm 1 g	270 \pm 1 g	90.0 \pm 1.2%
12 \pm 1 g	6 \pm 1 g	198 \pm 1 g	91.7 \pm 1.8%
12 \pm 1 g	6 \pm 1 g	304 \pm 1 g	94.4 \pm 1.2%
12 \pm 1 g	6 \pm 1 g	342 \pm 1 g	95.0 \pm 1.1%
12 \pm 1 g	6 \pm 1 g	382 \pm 1 g	95.5 \pm 1.0%

Table 12: Masses of resin, hardener, and tungsten carbide used in each sample, followed by each sample's percent tungsten carbide by mass.

Next, air dissolved in both the epoxy resin and epoxy hardener was removed using a bell jar evacuation chamber (see Figure 17). The cups and contents were placed in the bell jar evacuation chamber, the cover was secured, and the bell jar evacuation chamber was operated. Air bubbles began to rise to the surface of each liquid (see Figure 18 and 19), and when the bubble density began to decrease, the bell jar evacuation chamber was stopped. Then, the valve was opened to allow the interior of the bell jar evacuation chamber to return to atmospheric pressure, the cover was removed, and the cups and contents were removed.



Figures 17, 18, and 19 (left to right): The bell jar evacuation chamber, bubbles forming in the epoxy resin, and bubbles forming in the epoxy hardener.

each sample's volume calculated by its dimension measurements (see Table 13). A caliper was used to measure each sample's dimensions, and three measurements of each dimension were taken at different parts of the sample. The average of the three measurements was used for each dimension. Then, each sample's mass was divided by its volume to calculate its density (see Table 15 on next page).

The tungsten carbide powder was then poured into the epoxy resin, and the contents were stirred until they were completely mixed. The epoxy hardener was then added to the tungsten carbide powder and epoxy resin mixture, and the contents were again stirred until completely mixed. Then, before the hardening reaction began, the mold was uncovered at one end and the mixture was poured out into the mold until the mold was full. Because the 95% and 95.5% tungsten carbide by mass mixtures were so thick, the stirrer was used to overfill and pack the mixtures in their molds to ensure that there were no air pockets. Then, the rubber stopper was reinserted into the end of the mold. The sample was then clamped into a custom-made rotator (see Figure 20), and the rotator was operated until the sample hardened. The rotator was used to prevent the tungsten carbide powder from settling out before the sample hardened.



Figure 20: A sample rotating in the custom-made rotator

When the sample was completely hardened, it was removed from the rotator. The rubber stoppers were removed from the ends, and plastic tube exterior was slit with a blade and removed from the sample. The edges of each sample were buffed until approximately level, and the sample was then labeled with its percent tungsten carbide by mass. This procedure was repeated for each sample.

Measuring the Density of Each Sample

The density of each sample was required to calculate the acoustic impedance of each sample. To measure each sample's density, each sample's mass and volume had to be measured. The mass of each sample was measured by massing each sample twice on a scale and using the average reading (see Table 13). The volume used for each sample was the volume of water it displaced in a graduated cylinder (see Tables 14 and 15). This volume measurement was double-checked with

<u>Percent Tungsten Carbide by Mass</u>	<u>Mass Measurements</u>	<u>Average Mass</u>	<u>Diameter Measurements</u>	<u>Average Diameter</u>	<u>Length Measurements</u>	<u>Average Length</u>
0%	22 g, 24 g; all ± 1 g	23 ± 1 g	1.799 cm, 1.805 cm, 1.768 cm; all ± 0.001 cm	1.791 ± 0.001 cm	8.527 cm, 8.532 cm, 8.585 cm; all ± 0.001 cm	8.548 ± 0.001 cm
$60 \pm 4\%$	52 g, 52 g; all ± 1 g	52 ± 1 g	1.836 cm, 1.808 cm, 1.811 cm; all ± 0.001 cm	1.818 ± 0.001 cm	8.492 cm, 8.486 cm, 8.488 cm; all ± 0.001 cm	8.489 ± 0.001 cm
$70 \pm 3\%$	64 g, 64 g; all ± 1 g	64 ± 1 g	1.803 cm, 1.810 cm, 1.808 cm; all ± 0.001 cm	1.807 ± 0.001 cm	8.323 cm, 8.364 cm, 8.331 cm; all ± 0.001 cm	8.339 ± 0.001 cm
$80.0 \pm 2.3\%$	98 g, 98 g; all ± 1 g	98 ± 1 g	1.802 cm, 1.850 cm, 1.801 cm; all ± 0.001 cm	1.818 ± 0.001 cm	8.261 cm, 8.271 cm, 8.248 cm; all ± 0.001 cm	± 0.001 8.260 cm
$90.0 \pm 1.2\%$	140 g, 140 g; all ± 1 g	140 ± 1 g	1.814 cm, 1.796 cm, 1.793 cm; all ± 0.001 cm	1.801 ± 0.001 cm	8.271 cm, 8.252 cm, 8.273 cm; all ± 0.001 cm	± 0.001 8.265 cm
$91.7 \pm 1.8\%$	152 g, 152 g; all ± 1 g	152 ± 1 g	1.811 cm, 1.803 cm, 1.789 cm; all ± 0.001 cm	1.801 ± 0.001 cm	8.029 cm, 8.043 cm, 8.048 cm; all ± 0.001 cm	8.040 ± 0.001 cm
$94.4 \pm 1.2\%$	188 g, 188 g; all ± 1 g	188 ± 1 g	1.810 cm, 1.806 cm, 1.804 cm; all ± 0.001 cm	1.807 ± 0.001 cm	8.127 cm, 8.136 cm, 8.121 cm; all ± 0.001 cm	8.128 ± 0.001 cm
$95.0 \pm 1.1\%$	204 g, 204 g; all ± 1 g	204 ± 1 g	1.803 cm, 1.804 cm, 1.803 cm; all ± 0.001 cm	1.803 ± 0.001 cm	8.668 cm, 8.655 cm, 8.669 cm; all ± 0.001 cm	8.664 ± 0.001 cm
$95.5 \pm 1.0\%$	228 g, 228 g; all ± 1 g	228 ± 1 g	1.810 cm, 1.804 cm, 1.805 cm; all ± 0.001 cm	1.806 ± 0.001 cm	8.548 cm, 8.343 cm, 8.458 cm; all ± 0.001 cm	8.450 ± 0.001 cm

Table 13: Mass, diameter, and length measurements for each sample.

<u>Percent Tungsten Carbide by Mass</u>	<u>Initial water level</u>	<u>Final water level</u>
0%	60.9 ± 0.1 cm ³	82.5 ± 0.1 cm ³
$60 \pm 4\%$	59.1 ± 0.1 cm ³	80.9 ± 0.1 cm ³
$70 \pm 3\%$	69.0 ± 0.1 cm ³	90.1 ± 0.1 cm ³
$80.0 \pm 2.3\%$	45.0 ± 0.1 cm ³	66.1 ± 0.1 cm ³
$90.0 \pm 1.2\%$	60.6 ± 0.1 cm ³	81.5 ± 0.1 cm ³
$91.7 \pm 1.8\%$	61.0 ± 0.1 cm ³	81.6 ± 0.1 cm ³
$94.4 \pm 1.2\%$	55.7 ± 0.1 cm ³	76.3 ± 0.1 cm ³
$95.0 \pm 1.1\%$	59.9 ± 0.1 cm ³	82.0 ± 0.1 cm ³
$95.5 \pm 1.0\%$	58.0 ± 0.1 cm ³	79.8 ± 0.1 cm ³

Table 14: Initial and final water levels for each sample's water displacement test.

<u>Percent Tungsten Carbide by Mass</u>	<u>Dimension Volume</u> $\pi * \left(\frac{\text{diameter}}{2}\right)^2 * \text{length}$	<u>Displacement Volume</u> (final water level – initial water level)*cm ³ mL	<u>Density</u> $\frac{\text{average mass}}{\text{displacement volume}} * \frac{\text{kg}}{10^3 \text{g}} * \left(\frac{\text{m}}{10^2 \text{cm}}\right)^3$
0%	21.53 ±0.03 cm ³	21.6 ±0.02 cm ³	1.06 ±0.06 x10 ³ kg/m ³
60 ±4%	22.04 ±0.03 cm ³	21.8 ±0.02 cm ³	2.39 ±0.07 x10 ³ kg/m ³
70 ±3%	21.39 ±0.03 cm ³	21.1 ±0.02 cm ³	3.03 ±0.08 x10 ³ kg/m ³
80.0 ±2.3%	21.43 ±0.03 cm ³	21.1 ±0.02 cm ³	4.64 ±0.09 x10 ³ kg/m ³
90.0 ±1.2%	21.06 ±0.03 cm ³	20.9 ±0.02 cm ³	6.70 ±0.11 x10 ³ kg/m ³
91.7 ±1.8%	20.48 ±0.03 cm ³	20.6 ±0.02 cm ³	7.38 ±0.12 x10 ³ kg/m ³
94.4 ±1.2%	20.84 ±0.03 cm ³	20.6 ±0.02 cm ³	9.13 ±0.14 x10 ³ kg/m ³
95.0 ±1.1%	22.13 ±0.03 cm ³	22.1 ±0.02 cm ³	9.23 ±0.13 x10 ³ kg/m ³
95.5 ±1.0%	21.65 ±0.03 cm ³	21.8 ±0.02 cm ³	10.5 ±0.14 x10 ³ kg/m ³

Table 15: Dimension volume, displacement volume, and density calculation for each sample.

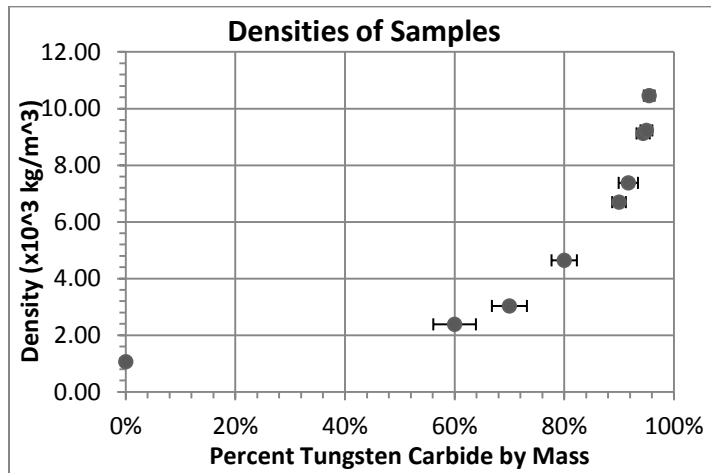


Figure 21: A graph of the densities of the test samples. As expected, a larger percent tungsten carbide by mass yielded a greater density.

Measuring the Speed of Sound through Each Sample

The speed of sound through each sample was also required to calculate the acoustic impedance of each sample. It was measured with an oscilloscope and a custom made “sono clamp,” a clamp which had a pulse-emitting transducer at one end and a pulse-receiving transducer at the other end (see Figure 22).

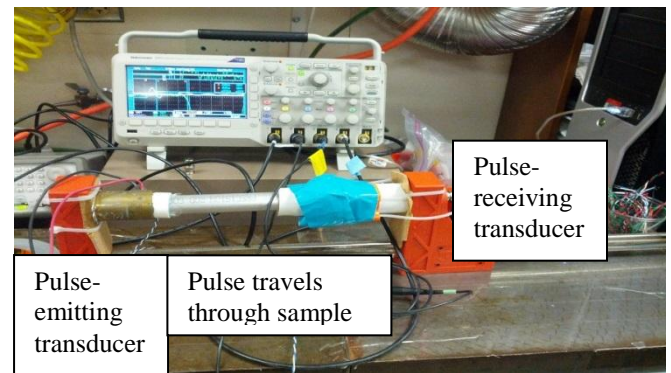


Figure 22: An aluminum sample being tested in the sono clamp.

To test a sample, coupling grease was spread on both ends of the sample, and the sample was inserted and secured into the sono clamp. A signal was sent to the emitting transducer, which converted the signal into a pulse. The pulse then traveled through the sample and to the receiving transducer, which converted the pulse back into a signal. The transducers were wired to the oscilloscope, and the signals were displayed on the oscilloscope screen (see Figure 23). The time interval on the oscilloscope was adjusted so it began when the emitting transducer sent the pulse, which was located at the zero of the largest fluctuation in the emitting transducer signal (purple), and ended when the receiving transducer received the pulse, which was located at the point where the slope of the receiving transducer signal (green) began to decrease. This time interval represented the time it took for sound to travel through the sample. The sample’s length (measured earlier) was then divided by the sample’s time interval to calculate the speed of sound through the sample.

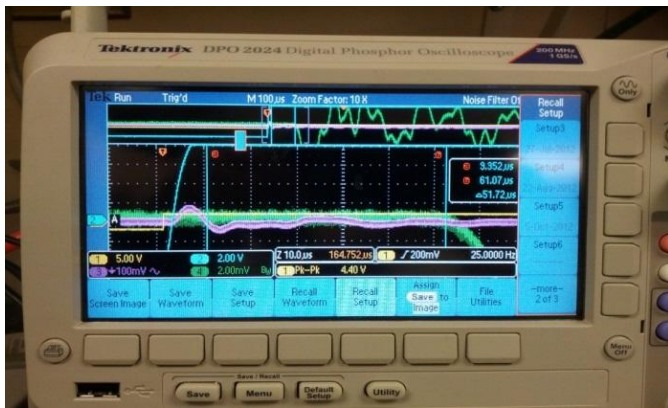


Figure 23: The oscilloscope reading when the 70% tungsten by mass sample was tested in the sono clamp.

Checking the Sono Clamp

First, the sono clamp was tested with an aluminum sample with a known speed of sound to make sure it was working properly. The length of the sample was measured with a caliper and divided by time interval to calculate the speed of sound through the sample. Then, the calculated speed of sound was compared to the known speed of sound. Since the percent error was so small, and the known speed of sound in aluminum fell within the uncertainty for the calculated speed of sound in the aluminum sample, the sono clamp was shown to be working properly. (See Table 16). The accuracy of this method was also tested by a previous student (Emily Grace 2011) who used it to measure the speed of sound in materials such as brass, aluminum, copper, acrylic and air. The device measures the speed of sound in these materials in agreement with accepted values with an uncertainty of 1%.

<u>Sample</u>	<u>Time Interval</u>	<u>Sample Length</u>	<u>Calculated Speed of Sound Through Sample</u>	<u>Known Speed of Sound Through Sample</u>	<u>Percent Error</u>
Aluminum	23.72 ±0.20 μs	14.960 ±0.001 cm	6307 ±54 m/s	6320 m/s	0.2070 %

Table 16: Speed of sound calculation for the aluminum sample.

Measuring the Speed of Sound through the Test Samples

The test samples were then tested with the sono clamp (using the same procedure as for the aluminum sample) to measure the time it took for the acoustic pulse to pass through each test sample (See Table 17).

<u>Percent Tungsten Carbide by Mass</u>	<u>Time Interval</u>	<u>Average Length</u>	<u>Speed of Sound Through Sample length of sample time interval</u>
0%	41.72 ±0.20μs	8.548 ±0.001 cm	2049 ±10 m/s
60 ±4%	49.72 ±0.20μs	8.489 ±0.001 cm	1707 ±7 m/s
70 ±3%	51.72 ±0.20μs	8.339 ±0.001 cm	1612 ±6 m/s
80.0 ±2.3%	57.72 ±0.20μs	8.260 ±0.001 cm	1431 ±5 m/s
90.0 ±1.2%	61.72 ±0.20μs	8.265 ±0.001 cm	1339 ±5 m/s
91.7 ±1.8%	52.92 ±0.20μs	8.040 ±0.001 cm	1519 ±6 m/s
94.4 ±1.2%	51.12 ±0.20μs	8.128 ±0.001 cm	1590 ±6 m/s
95.0 ±1.1%	53.72 ±0.20μs	8.664 ±0.001 cm	1613 ±6 m/s
95.5 ±1.0%	50.52 ±0.20μs	8.450 ±0.001 cm	1673 ±7 m/s

Table 17: Speed of sound calculations for each sample.

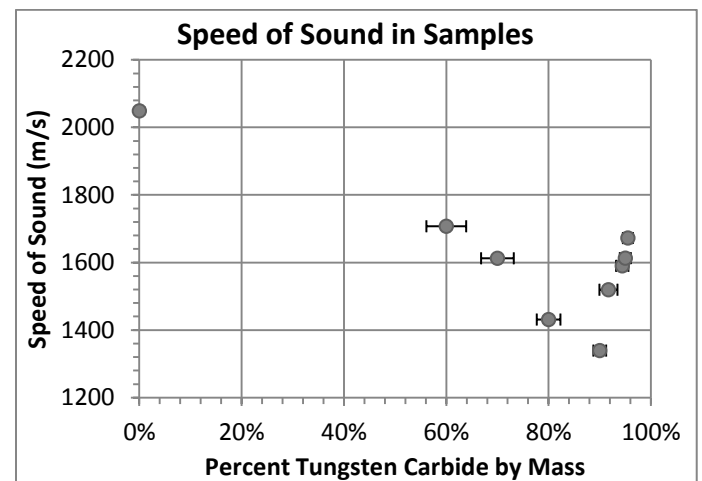


Figure 24: A graph of the speed of sound in the test samples.

The shape can be explained by the formula $v = \sqrt{\frac{E}{\rho}}$, where v is the speed of sound through a medium, E is the elastic modulus (a measure of the “stiffness” of the medium), and ρ is the density of the medium. The speed of sound initially decreases with increasing percent tungsten by mass because an increase in percent tungsten by mass causes a greater increase in density than stiffness. Later, however, the speed of sound increases with increasing density. This is probably because the tungsten particles begin to touch inside the mixture, greatly increasing the sample’s stiffness.

Calculating the Acoustic Impedance of Each Sample

Each sample’s acoustic impedance was calculated by multiplying its density by the speed of sound through the sample (see Table 18). As seen in Table 18 and Figure 25, the 95% tungsten by mass sample had an estimated acoustic impedance just 0.1 MRayl below the goal of 15 MRayl, and

the goal of 15 MRayl was included in the range when uncertainty was taken into account.

<u>Percent Tungsten Carbide by Mass</u>	<u>Density of Sample</u> avg mass displ.volume * $\frac{kg}{10^3g} * \left(\frac{m}{10^2cm}\right)^3$	<u>Speed of Sound Through Sample</u> length time $\frac{m}{10^2cm} * \frac{10^6\mu s}{s}$	<u>Acoustic Impedance (density) * (speed)</u> $\left(\frac{Rayl}{m^2s}\right) * \left(\frac{MRayl}{10^6Rayl}\right)$
0%	1.06 x10 ³ kg/m ³	2049 ±10 m/s	2.18 ±0.13 MRayl
60 ±4%	2.39 x10 ³ kg/m ³	1707 ±7 m/s	4.07 ±0.13 MRayl
70 ±3%	3.03 x10 ³ kg/m ³	1612 ±6 m/s	4.89 ±0.14 MRayl
80.0 ±2.3%	4.64 x10 ³ kg/m ³	1431 ±5 m/s	6.65 ±0.16 MRayl
90.0 ±1.2%	6.70 x10 ³ kg/m ³	1339 ±5 m/s	8.97 ±0.18 MRayl
91.7 ±1.8%	7.38 x10 ³ kg/m ³	1519 ±6 m/s	11.2 ±0.23 MRayl
94.4 ±1.2%	9.13 x10 ³ kg/m ³	1590 ±6 m/s	14.5 ±0.28 MRayl
95.0 ±1.1%	9.23 x10 ³ kg/m ³	1613 ±6 m/s	14.9 ±0.27 MRayl
95.5 ±1.0%	10.5 x10 ³ kg/m ³	1673 ±7 m/s	17.5 ±0.31 MRayl

Table 18: Acoustic impedance calculation for each sample

Converting to Percent Tungsten by Volume

In keeping with standard methods, the percent tungsten carbide by mass was converted to percent tungsten by volume (see Table 19, and Figures 29, 31, and 31) using $\chi_{TV} = \frac{1.1\chi_{TM}}{15.8-14.7\chi_{TM}}$, where χ_{TV} is percent tungsten carbide by volume and χ_{TM} is percent tungsten carbide by mass.

Derivation of tungsten carbide volume fraction in terms of tungsten carbide mass fraction:

$$\chi_{TV} = \frac{V_T}{V_S} = \frac{m_T/\rho_T}{m_S/\rho_S} = \frac{\chi_{TM}\rho_S}{\rho_T} = \frac{\chi_{TM}}{\rho_T} \left(\frac{\rho_T\rho_E}{\chi_{TM}(\rho_E - \rho_T) + \rho_T} \right) = \frac{\chi_{TM}\rho_E}{\chi_{TM}(\rho_E - \rho_T) + \rho_T}$$

With $\rho_T = 15.8 \text{ g/cm}^3$ and $\rho_E = 1.1 \text{ g/cm}^3$, $\chi_{TV} = \frac{1.1\chi_{TM}}{15.8-14.7\chi_{TM}}$

<u>Percent Tungsten Carbide by Mass</u>	<u>Percent Tungsten Carbide by Volume</u>
0%	0%
60 ±4%	9.5 ±1.5%
70 ±3%	14.0 ±2.0%
80.0 ±2.3%	21.8 ±2.7%
90.0 ±1.2%	38.5 ±3.5%
91.7 ±1.8%	43.5 ±6.4%
94.4 ±1.2%	54.0 ±6.2%
95.0 ±1.1%	56.9 ±6.1%
95.5 ±1.0%	59.6 ±5.9%

Table 19: Percent tungsten carbide by volume for each sample.

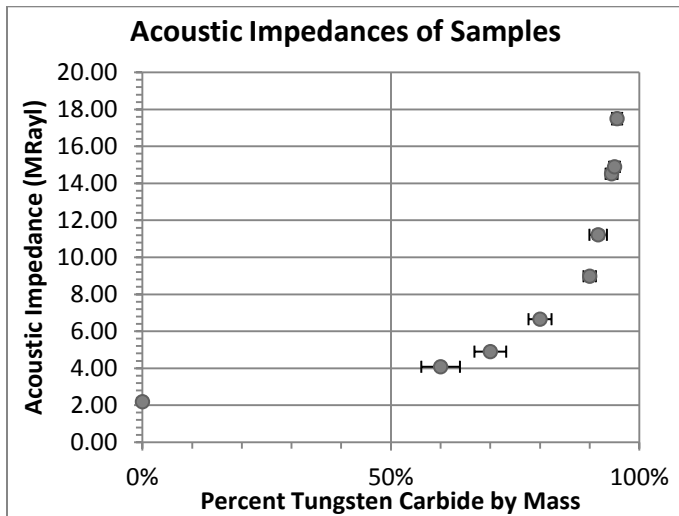


Figure 25: A graph of the acoustic impedances of the test samples. As expected, a higher percent tungsten carbide by mass resulted in a greater acoustic impedance.

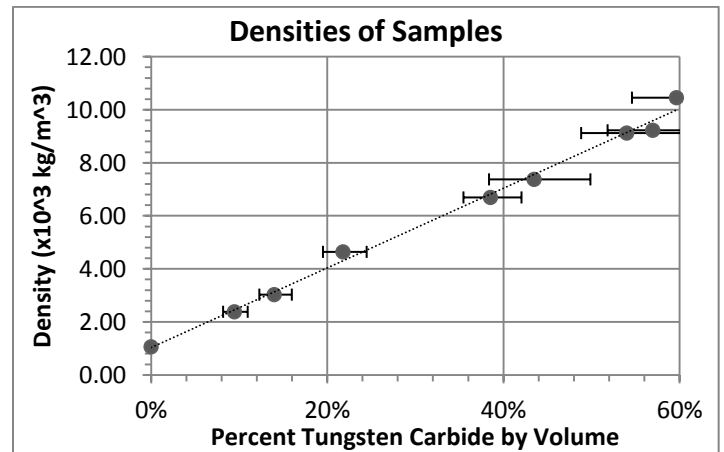


Figure 26: A graph of the percent tungsten carbide by volume of the samples vs. the density of the samples.

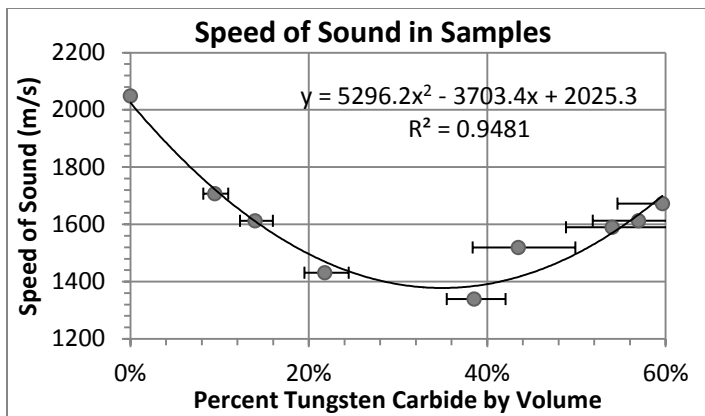


Figure 27: A graph of the percent tungsten carbide by volume for each sample vs. the speed of sound through each sample.

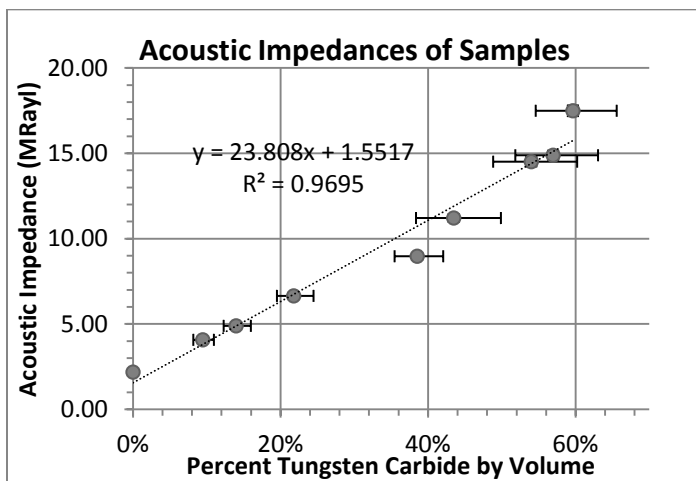


Figure 28: A graph of the percent tungsten carbide by volume for each sample vs. the acoustic impedance for each sample.

The relationship between impedance and volume fraction appeared to be linear, so a linear regression was used to determine a relationship between acoustic impedance and percent tungsten carbide by volume. This relationship was used to determine the proportion of tungsten carbide to epoxy mixture needed to create a sample with any desired acoustic impedance.

The acoustic impedance of the laboratory pz-27 transducer was 23.5 MRayl, and using the same method as for the samples, the acoustic impedance of the laboratory glass was measured to be 8.26 MRayl. The goal impedance was then $\sqrt{23.5 * 8.26} = 13.9$ MRayl.

Making the Wafer for the Matching Layer

Because the 93.9% tungsten carbide by mass (51.9% tungsten carbide by volume) sample had an acoustic impedance of 13.9 MRayl using the linear regression, a wafer was cut from the sample and tested to see whether it improved transducer sensitivity.

Determining the Correct Thickness

In order for the wafer to couple correctly to the transducer, its thickness needed to be one fourth the wavelength of the propagated sound wave. Because the transducer was chosen so that its resonant frequency matched the frequency of the bubbles' acoustic emissions, the resonant frequency of the transducer was used to calculate the wavelength of the propagated sound (see Table 21). To measure the resonant frequency of the transducer, a Welch Power Spectrum graph was created for the selected transducer.

The Welch Power Spectrum, like a Fast Fourier Transform, plots the power of a signal over a range of frequencies. To create a Welch Power Spectrum for a transducer, the transducer was tested in the "sound detonator," a box with an air source. The transducer was connected to the oscilloscope and placed on a sponge block so it was level to the air source (see Figure 29). The sound detonator was then closed, and the air valve was opened to let pressurized air blow on the transducer. The oscilloscope settings were adjusted so the wave was as large as possible without "clipping," or exceeding the top or bottom edges of the display. The waveform was saved on the oscilloscope, and the wave data was used to create a Welch Power Spectrum in MATLAB.



Figure 29: The sound detonator setup for a transducer (a different transducer was actually used when data was taken)

To make sure the Welch Power Distribution method was accurate, Welch Power Distributions were created for a copper sample and an aluminum sample. The length of each sample was measured with a caliper, and since the speeds of sound through copper and aluminum are known, the length and speed of sound through the sample were used to calculate the resonant frequency of the sample. This calculated resonant frequency was compared to the resonant frequency indicated by the peak on each sample's Welch Power Distribution (see Figure 30 and Table 20). A 50% tungsten carbide by volume sample from a different experiment was also tested because it had a known resonant frequency.

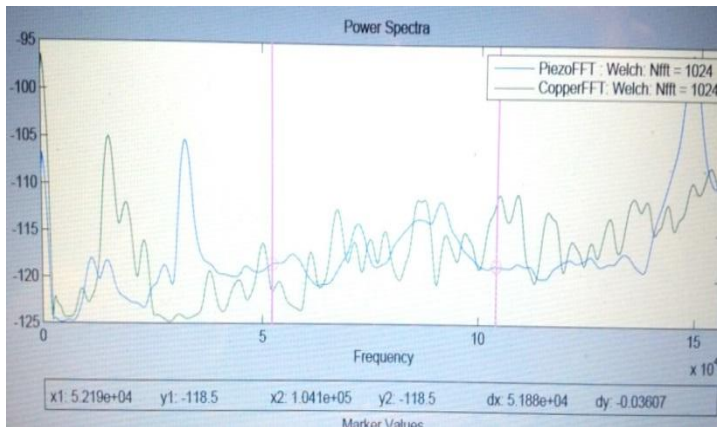


Figure 30: The Welch Power Spectrum of the copper sample and transducer (green) and the transducer by itself (blue).

Sample	Speed of Sound Through Sample	Length of Sample	Calculated Resonant Frequency	Peak on WPD
Copper	4600-4700 m/s	0.1488 m	15-16 kHz	15 kHz
Aluminum	5000-6500 m/s	.150 m	16-22 kHz	16.5 kHz
50% Tungsten carbide by mass	-	-	12 kHz (different experiment)	12 kHz

Table 20: Calculated resonant frequency and frequency peak on Welch Power Distribution for each sample

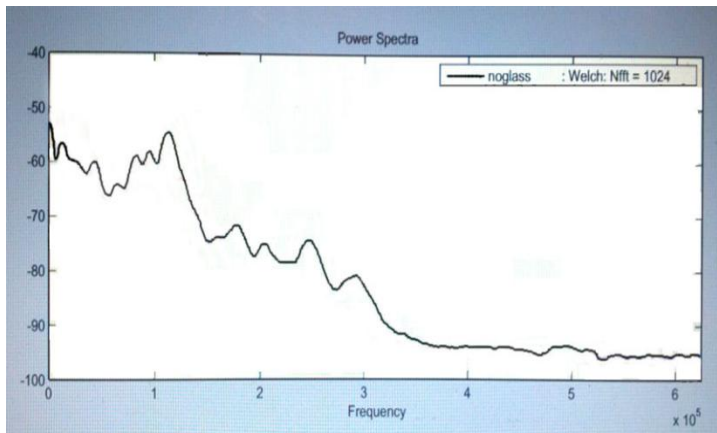


Figure 31: The Welch Power Spectrum of the transducer. The resonant peak is seen at 111 kHz.

Calculated Quantity	Calculation	Result
Goal thickness	$\frac{\lambda}{4} = \frac{1}{4} * \frac{\text{speed of sound}}{\text{resonant frequency}}$	3.4 mm

Table 21: Calculation of the goal thickness for the wafer.

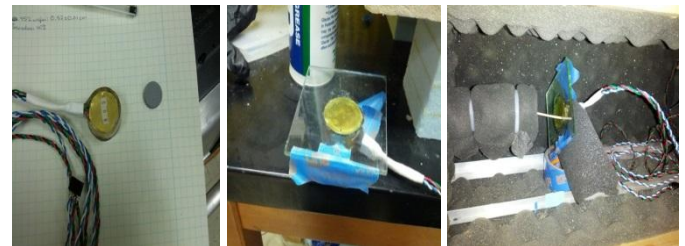
Cutting the Wafer

The wafer was cut using a saw in a plastic apparatus which ensured the cut was straight. Then, the wafer was sanded to the correct thickness. The thickness of the wafer was 3.4 ± 0.1 mm.

Testing the Wafer

To test the wafer, a WPD was first conducted for the transducer with a layer of glass using the same procedure as for the transducer alone. The wafer was then placed between a layer of glass and the selected transducer (transducer #403). Glacier grease was used to couple the mediums, and tape was used to hold the media together (see Figures 32, 33, and 34). A WPD was then created for the transducer, wafer, and glass.

Surprisingly, inserting the wafer between the glass and the transducer severely damped the signal rather than amplifying the resonant frequency of the transducer. To test whether this result could have been caused by the type of glass used, two other glass squares of different thicknesses were tested with the transducer as well (see Figure 35). Since the WPDs for all three glass squares were very similar near the resonant frequency of the transducer (see Figure 36), the type of glass used could not account for the dampened signal.



Figures 32, 33, and 34 (left to right): The matching layer and transducer #403, the transducer coupled to the glass outside of the sound detonator, and the transducer coupled to the glass inside the sound detonator.

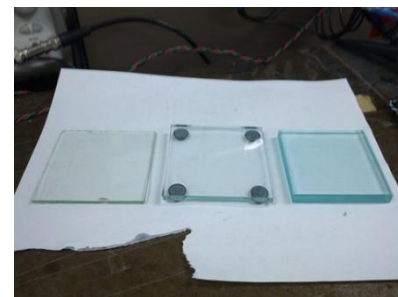


Figure 35: Three glass squares, each of different thickness. From left to right, the thicknesses are 3.15mm, 5.70mm, and 9.40mm.

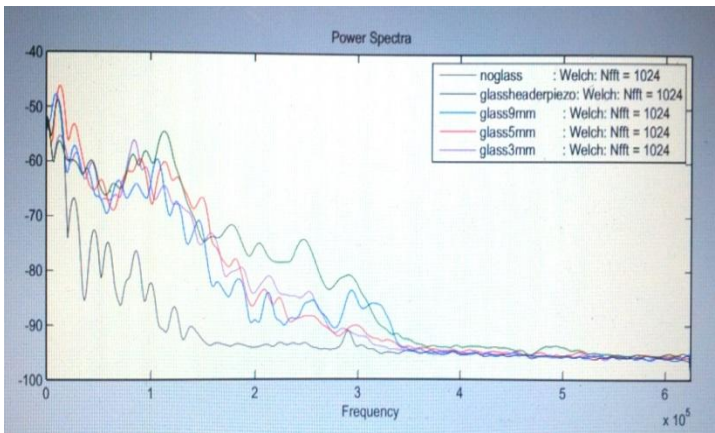


Figure 36: Welch Power Distributions for the transducer alone (green), the transducer with a layer of glass and the wafer (grey), the transducer with the 9.40mm glass square (blue), the transducer with the 5.70mm glass square (red), and the transducer with the 3.15mm glass square (violet). The resonant frequency of the transducer is at 111 kHz, and all the glass samples seem to have similar curves near the 111 kHz area. However, the addition of the wafer caused the signal to lose a lot of power.

Making the Larger Wafer

Another reason for the dampened signal could be that the wafer did not completely cover the transducer. To test this explanation, a larger 95% sample was made. The procedure was the same as for the smaller samples, except that a pill jar was used rather than a plastic tube in order to make the diameter of the sample larger.



Figure 37: The unhardened 95% sample in the bell jar evacuation chamber.

Testing the Larger Wafer

The larger wafer was tested using the same procedure as for the smaller wafer. As seen in Figure 38, the effect of the larger wafer was very similar to that of the smaller wafer: rather than amplifying the transducer's resonant frequency of 111 kHz, the wafer resulted in damping.

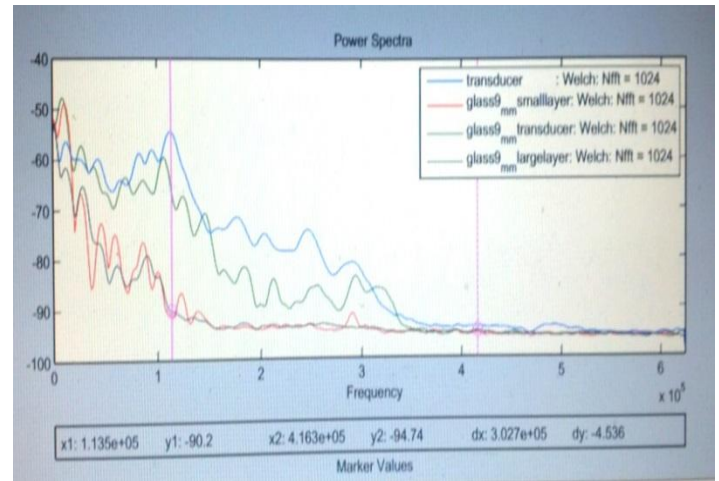


Figure 38: Welch Power Distributions for the transducer alone (blue), the transducer with the 9.40mm glass square (green), the transducer with the small wafer and the 9.40mm glass square (red), and the transducer with the large wafer and the 9.40mm glass square (grey). Like the smaller wafer, the larger wafer caused the signal to lose a lot of power.

Conclusions

One possible reason that the tungsten carbide powder and epoxy composite attenuated the sound wave is that there may have been tiny air pockets in the composite. Even though dissolved air was removed from the mixture with the bell jar gas evacuation chamber, air may have been reintroduced into the mixture when it was packed into the mold. Air pockets would have created density fluctuations, which would have led to acoustic impedance fluctuations, resulting in significant reflection and scattering.

Another possible explanation for the damped signal is that the tungsten carbide powder and epoxy composite used in this project may not be effective as a matching layer. Although the effective speed of sound through a tungsten carbide powder and epoxy sample is known, there are actually many variations due to the fact that the sample is a mixture. An effective matching layer might require a structured crystalline lattice rather than tiny flakes of tungsten carbide suspended in epoxy. To address this, one should attempt to make a matching layer using a metal with an acoustic impedance close to 13.9MRayl.

Although the tungsten carbide powder and epoxy composite used in this project might not be an ideal matching layer material, its attenuating properties do have other applications. The composite will be used for a backing layer for the acoustic transducers in the COUPP experiment. A backing layer is used to decrease transducer ringing by absorbing sound once it has already traveled to the transducer, thereby improving resolution.

Acknowledgements

I am indebted to Dr. Ilan Levine, professor at Indiana University South Bend, for serving as my mentor and allowing me to use his laboratory for this project.

I am also obliged to Mr. Edward Behnke, Mr. Thomas Nania, Mr. Cale Harnish, and Mr. Adam Behnke of Indiana University South Bend for advice and assistance in the laboratory, and to Indiana University South Bend itself for providing a laboratory and many of the materials necessary for this project.

I also owe thanks to Mr. Ken Andrzejewski and Dr. Doug Sisk for assistance in developing scientific thinking and entering this project in various competitions.

Last, but not least, I must thank the Indiana Academy of Science for a Junior Research Grant.

References

- [1] Bennett, Jeffery, et al. *The Cosmic Perspective*. 3rd ed. San Francisco: Addison Wesley, 2004. 679-696. Print.
- [2] Knill, Oliver. "Zwicky, Fritz." (2006): 1. Web. 29 Sept 2012.
- [3] *Rotation Curve for the Milky Way Galaxy*. 2010. Chart. University of Oregon Department of Physics: Astronomy 123. Web. 13 Oct 2012. <http://physics.uoregon.edu/~jimbrau/BrauImNew/Chap23/6th/23_21Figure-F.jpg>.
- [5] *Einstein Ring Gravitational Lens*. N.d. Photograph. HubbleSite. Web. 13 Oct 2012. <<http://hubblesite.org/gallery/album/pr2005032g/>>.
- [6] NASA/WMAP Science Team. *Five Year Microwave Sky*. N.d. Photograph. National Aeronautics and Space Administration. Web. 14 Oct 2012.
- [7] Fry, Alexander. "Dark Matter Confronts Observations." *The Astronomist*. N.p. 4 May 2010. Web. 29 Sept. 2012.
- [8] Profumo, Stefano. "Fundamental Physics from the Sky: Cosmic Rays, Gamma Rays, and the Hunt for Dark Matter." *18th International Symposium on Particles, Strings and Cosmology (PASCOS 2012)* (2012): n.pag. *ArXiv*. Database. 29 Sept. 2012.
- [9] Hooper, Dan, and Tim Linden. "Gamma Rays From The Galactic Center and the WMAP Haze." *Phys.Rev.D* 83. (2011): n.pag. *ArXiv*. Database. 28 Sept. 2012.
- [10] NASA/WMAP Science Team. "Fluctuations in the Cosmic Microwave Background." *National Aeronautics and Space Administration*. N.p. 10 Dec. 2012. Web. 29 Sept. 2012.
- [11] "Evidence for Dark Matter." *Chandra X-ray Observatory*. N.p. 13 May 2012. Web. 29 Sept. 2012.
- [12] NASA/WMAP Science Team. "The WMAP Achievement." *National Aeronautics and Space Administration*. N.p. 16 April 2010. Web. 29 Sept. 2012.
- [13] Massey, Richard, Thomas Kitching, et al. "The dark matter of gravitational lensing." *Rep. Prog. Phys.* 73. (2010): n.pag. *ArXiv*. Database. 28 Sept. 2012.
- [14] NASA/WMAP Science Team. *Tests of Big Bang: The Light Elements*. N.d. Chart. National Aeronautics and Space Administration. Web. 14 Oct 2012.
- [15] Copi, Craig J., David N. Schramm, et al. "Big-Bang Nucleosynthesis and the Baryon Density of the Universe." *Science* 267. (1995): 192-199. *ArXiv*. Database. 29 Sept. 2012.
- [16] Grocutt, Emma. "What is Dark Matter?." *CFHTLenS*. N.p., n.d. Web. 6 Oct 2012. <<http://www.cfhtlens.org/public/what-dark-matter>>
- [17] Chaisson, Eric and Steve McMillan. "Chapter Review." *Castle Rock*. N.p. Web. 29 Sept. 2012. <<http://www.castlerock.wednet.edu/HS/stello/Astronomy/TEXT/CHAISSON/BG317/HTML/BG317EOC.htm>>
- [18] Rees, Martin J. "Dark Matter: Introduction." *Phil.Trans.Roy.Soc.Lond.* 361. (2003): 2427-2434. *ArXiv*. Database. 13 Oct 2012.
- [19] XENON Collaboration, . *The XENON Dark Matter Project*. Columbia University, 17 2011. Web. Web. 26 Oct. 2012. <<http://xenon.astro.columbia.edu/>>.
- [20] *Super Cryogenic Dark Matter Search*. University of California, Berkeley, n. d. Web. Web. 20 Oct. 2012. <<http://cdms.berkeley.edu/CDMSII.html>>.
- [21] *The Picasso Experiment*. N.p., n. d. Web. Web. 13 Oct. 2012. <<http://www.picassoexperiment.ca/dm.php>>.
- [22] *COUPP Experiment - E961*. COUPP Collaboration, 8 Dec. 2006. Web. 26 Oct. 2012. <<http://www-coupp.fnal.gov/>>.
- [23] Bennett, Jeffery, et al. *The Cosmic Perspective*. 3rd ed. San Francisco: Addison Wesley, 2004. 679-696. Print.
- [24] Massey, Richard, Thomas Kitching, et al. "The dark matter of gravitational lensing." *Rep. Prog. Phys.*

73. (2010): n.pag. *ArXiv*. Database. 28 Sept. 2012.
- [25] Cline, David B. "The Search for Dark Matter." *Scientific American*. 52-59. March 2003. Print. 20 Sept. 2012.
- [26] Tro, Nivaldo J. *Chemistry: a Molecular Approach*. 2nd ed. Upper Saddle River: Pearson Education, Inc., 2011. 289-90. Print.
- [27] Behnke, E., J. Behnke, et al. "First dark matter search results from a 4-kg CF₃I bubble chamber operated in a deep underground site." *Phys. Rev. D*. 86. (2012): 933-936. *ArXiv*. Database. 4 Oct. 2012.
- [28] "Experiment." *The Picasso Experiment*. N.p., n.d. Web. 13 Oct 2012.
<www.picassoexperiment.ca/experiment.php>
- [29] XENON100 Collaboration, . "The XENON100 Dark Matter Experiment." *Astropart. Phys.* 35. (2012): 573-590. *ArXiv*. Database. 13 Oct 2012.
- [30] XENON100 Collaboration, . "Dark Matter Results from 100 Live Days of XENON100 Data." *Phys. Rev. Lett.* 107. (2011): 573-590. *ArXiv*. Database. 13 Oct 2012.
- [31] Giboni, K. L., E. Aprile, et al. "Xenon Recirculation-Purification with a Heat Exchanger." *JINST* 6. (2011): 573-590. *ArXiv*. Database. 13 Oct 2012.
- [32] Aprile, Elena. "The XENON1T: Experiment at LNGS." DM2012. 24 Feb. 2012. <http://xenon.astro.columbia.edu/talks/XENON1T_DM2012_Elena.pdf>.
- [33] *CDMS II Detectors*. University of California, Berkeley, 28 Apr. 2007. Web. 22 Oct. 2012.
<<http://cdms.berkeley.edu/Education/DMpages/science/detectors.shtml>>
- [34] Davour, A. "The PICASSO Dark Matter Search Project." *Proc. of Identification of Dark Matter 2008*(2010): n.pag. *The Picasso Experiment*. 28 Sept. 2012.
- [35] Conner, Austin. *Design, Construction, and Commissioning of a COUPP Pressure Vessel Simulator*. (2011): 1-11. Web. 20 Sept. 2012.
- [36] Collar, Juan, Eric C. Dahl, et al. "COUPP *-500: A Proposal for a Ton Scale Bubble Chamber for Dark Matter Detection." (2010): 1,3,30. *Coupp Experiment-E961*. Web. 26 Oct 2012.
- [37] Behnke, E., J.I. Collar, et al. "Improved Spin-Dependent WIMP Limits from a Bubble Chamber." *Science*. 319. (2008): 933-936. *ArXiv*. Database. 20 Sept 2012.
- [38] Behnke, E., J. Behnke, et al. "First dark matter search results from a 4-kg CF₃I bubble chamber operated in a deep underground site." *Phys. Rev. D*. 86. (2012): 933-936. *ArXiv*. Database. 4 Oct. 2012.
- [39] *Sound Waves in Air*. N.d. HyperPhysics. Web. 5 Nov 2012. <<http://hyperphysics.phy-astr.gsu.edu/hbase/sound/tralon.html>>.
- [40] *S-Wave*. N.d. ESG Solutions. Web. 7 Nov 2012. <<http://www.esgsolutions.com/english/view.asp?x=857>>.
- [41] *Rayleigh wave motion process*. 2004. SPICE Research Training Network and the University of Oslo. Web. 5 Nov 2012.
<<http://folk.uio.no/valeriem/spice/Frame/surfacew/index.html>>
- [42] "Introduction to Ultrasonic Testing." *NDT Resource Center*. N.p. Web. 22 Oct 2012. <http://www.ndt-ed.org/EducationResources/CommunityCollege/Ultrasonics/cc_ut_index.htm>.
- [43] N.d. NDT Resource Center. Web. 5 Nov 2012. <<http://www.ndt-ed.org/EducationResources/CommunityCollege/Ultrasonics/Physics/modepropagation.htm>>.
- [44] Baun, Jim. *Physical Principles of General and Vascular Sonography*. 24-34. Web. 25 Oct. 2012. <http://www.jimbaun.com/2_interaction_softissue.pdf>.
- [45] Dukhin, A. S., P. J. Goetz, et al. "Use of Ultrasound for Characterizing Dairy Products." *Journal of Dairy Science* 88.4 (2005): 1320-1334. *ScienceDirect*. Database. 11 Dec 2012.
<<http://www.sciencedirect.com/science/article/pii/S0022030205727983>>.
- [45] "Energy Threshold." *The Picasso Experiment*. N.p., n.d. Web. 13 Oct 2012.
- [46] "Sound Propagation." *HyperPhysics*. Georgia State University. Web. 22 Oct 2012.
<<http://hyperphysics.phy-astr.gsu.edu/hbase/sound/sprop.html>>
- [47] *FFT*. N.d. Studio Six Digital. Web. 7 Nov 2012. <<http://www.studiosixdigital.com/audiotools/fft/>>
- [48] "Sound Measurement." *HyperPhysics*. Georgia State University. Web. 23 Oct 2012.
<<http://hyperphysics.phy-astr.gsu.edu/hbase/sound/sprop.html>>
- [49] Zielinski, Tomasz G. *Fundamentals of Piezoelectricity*. Institute of Fundamental Technological Research. Web. 24 Oct 2012.
<http://www.ippt.gov.pl/~tzielins/doc/ICMM_TG_Zielinski_Piezo.slides.pdf>.
- [50] "What's a Transducer?." *APC International, Ltd.*. Institute of Fundamental Technological Research. Web. 24 Oct 2012.
<<http://www.americanpiezo.com/piezo-theory/whats-a-transducer.html>>.
- [51] Wolfe, Joe. "dB: What is a decibel?." *Physclips*. School of Physics UNSW, n. d. Web. Web. 7 Nov. 2012.
<<http://www.animations.physics.unsw.edu.au/jw/dB.htm>>.